Cavity filling with shear-thinning liquids

Jyun-Ting Wu,[1] Lorraine F. Francis,[1] Marcio S. Carvalho,[2] and Satish Kumar[1]
[1]*Department of Chemical Engineering and Materials Science, University of Minnesota, Minneapolis, Minnesota 55455, USA*
[2]*Department of Mechanical Engineering, Pontifícia Universidade Católica do Rio de Janeiro, Rio de Janeiro, RJ 22451-900, Brazil*

(Received 16 October 2019; accepted 14 April 2020; published 19 May 2020)

The filling of small cavities with liquids plays a central role in numerous settings including imprint lithography, gravure printing, microfluidics, lubricant-impregnated surfaces, and porous-media flow. Air entrapment resulting from incomplete filling may be detrimental for certain applications. Although wetting dynamics can be complicated by liquid rheology, the influence of non-Newtonian behavior is not well understood. To develop fundamental understanding, two-dimensional numerical simulations are used to study liquid filling in two model problems involving a stationary trapezoidal cavity and a horizontal plate above the cavity. In these model problems, liquid is driven into the cavity by (i) an imposed pressure gradient and (ii) a combination of horizontal plate motion and an imposed pressure gradient. Shear-thinning liquids described by a Carreau-type expression are considered, and the nonlinear governing equations with inertia and gravity neglected are solved using the Galerkin finite-element method. For both model problems, it is found that increasing cavity width and wettability, decreasing wall steepness, or lowering the capillary number generally improves filling by allowing the contact line on the cavity to slip more. Shear thinning enhances contact-line motion via reduced viscosities near the dynamic contact line and, as a consequence, leads to improved cavity filling.

DOI: 10.1103/PhysRevFluids.5.054003

I. INTRODUCTION

Liquid filling of recessed features having micro- to nanometer scales plays a key role in various settings such as imprint lithography [1–4] and gravure printing (Fig. 1) [5]. Incomplete filling could lead to entrapment of air, which may cause bubble-type defects in printed/imprinted structures, compromising device functionality and reproducibility [6–11]. Feature filling is also highly relevant to other applications including microfluidics [12–14], lubricant-impregnated surfaces [15–17], and porous-media flow [18–21].

Whether recessed features are completely filled depends on the movement of three-phase contact lines and the deformation of the liquid-air interface [22,23]. In general, wetting dynamics are strongly influenced by feature shapes [24–29] and can be complicated by non-Newtonian rheology [30]. This paper seeks to better understand filling of non-Newtonian liquids to provide a foundation for designing liquid rheology in practical applications.

The present paper focuses on two important model problems concerning cavity filling shown in Fig. 2, where a mass of liquid is driven into the gap between a trapezoidal cavity and a flat plate. In the first configuration [Fig. 2(a)], both surfaces are stationary and the flow is driven by a pressure gradient. This configuration serves as a simple model of the filling process in imprint lithography [31] and is relevant to microfluidic [13,14] and porous-media flows [18–20]. In the second configuration [Fig. 2(b)], the flat plate moves horizontally above a stationary cavity and the flow is driven by the plate motion and a pressure gradient. This configuration serves as a

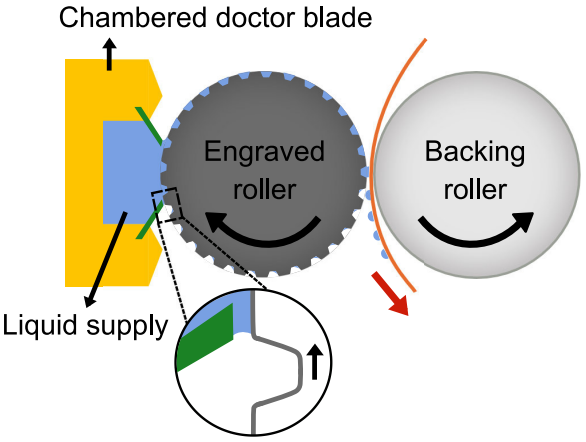

FIG. 1. Schematic of a chambered doctoring system in a gravure process: liquid is filled into cavities on an engraved roller and the excess liquid is wiped off by a doctor blade [5].

simple model for cavity filling in a chambered doctoring system (Fig. 1) and can be connected to nanoimprinting [11]. We note that filling of partially filled cavities could also be an important issue because liquid in the cavities may not be completely emptied in actual gravure processes with continuous operation [10].

Although an array of features is typically used in practice [10,32,33], the model problems considered here provide a rational basis for understanding the interactions between flows in adjacent features. We also note that while the dynamics of contact-line motion can be influenced by three-dimensional (3D) effects [34–36], the study of two-dimensional (2D) flows is useful for building physical understanding and is less computationally intensive.

Liquid filling of rectangular cavities in a configuration similar to that shown in Fig. 2(a) was studied by Reddy *et al.* [31] using finite-element simulations. They focused on Newtonian liquids, and observed that complete filling can be achieved for cavities where the width-to-depth ratio is sufficiently large. This is attributed to a rapid reconfiguration of the liquid-air interface when the moving contact line reaches the far bottom corner of the cavity. Kim *et al.* [37] studied the effects of surface wettability on cavity filling in a similar configuration using a volume-of-fluid method. They found that decreasing the contact angle allows liquid to fill more of the cavity, reducing air entrapment. Similar findings were reported by Morihara *et al.* [38] using finite-difference simulations.

Volume-of-fluid simulations were conducted by Peng *et al.* [39] to study filling of Newtonian liquids into pyramid-shaped cavities. They found that the amount of entrapped air is reduced with lower injection speed, lower liquid viscosity, and smaller confinement between the cavity and

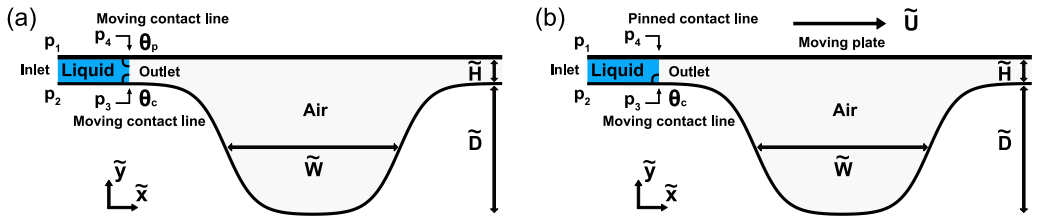

FIG. 2. Schematics of model geometries considered in this paper: filling of liquid between a stationary cavity and (a) a stationary flat plate and (b) a flat plate moving horizontally. Corner points p_1, p_2, p_3, and p_4 denote the initial positions of the liquid domain.

flat surface. They noted that the shape and location of air bubbles are highly associated with the orientation of the pyramid structure relative to the injected liquid.

Cen *et al.* [34] studied filling of Newtonian liquids in a configuration similar to that shown in Fig. 2(b). They performed visualization experiments with an array of pyramid-shaped cavities and observed that complete filling becomes more difficult when the capillary number, Ca (the ratio of viscous forces to surface-tension forces), increases. They indicated that complete filling can be realized for $\mathrm{Ca} < O(10^{-1})$ while pronounced air entrapment arises at $O(1)$ values of Ca owing to strong contact-line pinning near the structure edges. These observations are qualitatively described by their 3D finite-element simulations using a single cavity.

The present paper has two key motivations. First, although the prior work discussed above covers a range of physical parameters affecting cavity filling for Newtonian liquids, the influence of cavity wall steepness has not been reported. The extent of wall inclination is of practical importance and can affect contact-line motion significantly [40,41]. As contact-line motion is related to the distribution of pressure gradients, it is also of interest to characterize how these gradients are influenced by wall inclination and liquid rheology. Second, although non-Newtonian rheology is important in practical applications, its influence on cavity filling has not been addressed. In this paper, we investigate liquids displaying shear thinning, which is among the most common rate-dependent rheological properties. We use a Carreau-type expression to describe shear thinning, and examine how the extent of shear thinning influences cavity filling and the associated pressure gradients. Although we focus on liquid filling between two solid surfaces, the findings regarding the influence of liquid rheology on contact-line motion are more generally applicable to other filling problems without confined boundaries [15–17,42,43].

The problem formulation is described in Sec. II. Cavity filling driven purely by an imposed pressure gradient [Fig. 2(a)] is studied in Sec. III, followed by the case of cavity filling driven by combined plate motion and an imposed pressure gradient [Fig. 2(b)] in Sec. IV. Conclusions are presented in Sec. V.

II. PROBLEM FORMULATION

A. Governing equations

We consider an incompressible liquid with density $\tilde{\rho}$, surface tension $\tilde{\sigma}$, and viscosity $\tilde{\mu}$, where $\tilde{\mu}$ may depend on a scalar measure of the deformation rate, $\tilde{\dot{\gamma}}$. The liquid is confined between a stationary trapezoidal cavity with depth $\tilde{D}$ and width $\tilde{W}$ and a flat plate that is kept stationary [Fig. 2(a)] or moved horizontally at velocity $\tilde{U}$ [Fig. 2(b)] above the cavity. The spacing between the cavity and plate is $\tilde{H}$. Similar geometries have been used for studying cavity emptying with non-Newtonian liquids [44,45]. In this paper, variables with tildes represent dimensional quantities.

To define the cavity geometry, two hyperbolic tangent functions are used [45]:

$$\tilde{y} = 1 + \frac{1}{2}\tilde{D}\left[\tanh\left(\frac{\tilde{x} - \tilde{r}_c}{\tilde{r}_s}\right) - \tanh\left(\frac{\tilde{x} - \tilde{r}_c + \tilde{\delta}}{\tilde{r}_s}\right)\right], \tag{1}$$

where $\tilde{x}$ and $\tilde{y}$ are the horizontal and vertical positions along the cavity wall, $\tilde{r}_c$ is related to the distance from the cavity symmetry plane to the center of the wall, $\tilde{r}_s$ determines the roundness of the corners and the steepness of the cavity wall (e.g., Fig. 3), and $\tilde{\delta}$ controls the cavity width such that $\tilde{W} = \tilde{\delta}$. By using hyperbolic tangent functions, Eq. (1) gives a smooth and continuous cavity shape, which is convenient for numerical simulations. The resulting cavity shape is like a trapezoid, which is relevant for practical applications [10].

By scaling length with cavity depth $\tilde{D}$, time with $\tilde{D}/\tilde{U}_c$, and pressure with $\tilde{\mu}_0\tilde{U}_c/\tilde{D}$, where $\tilde{U}_c$ is the characteristic velocity and $\tilde{\mu}_0$ denotes the viscosity at zero deformation rate, two dimensionless parameters are defined: a Reynolds number $\mathrm{Re} = \tilde{\rho}\tilde{U}_c\tilde{D}/\tilde{\mu}_0$, which is the ratio of inertial to viscous forces, and a Stokes number $\mathrm{St} = \tilde{\rho}\tilde{g}\tilde{D}^2/\tilde{\mu}_0\tilde{U}_c$, which is the ratio of gravitational to viscous forces,

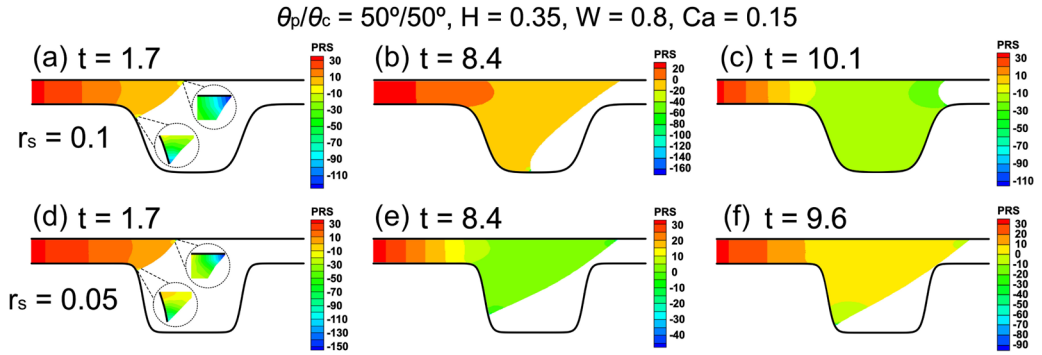

FIG. 3. Contours of dimensionless pressure for Newtonian liquids being filled into cavities with $\theta_p/\theta_c = 50^\circ/50^\circ$, $H = 0.35$, $W = 0.8$, and Ca $= 0.15$ at different times: (a–c) $r_s = 0.1$ and (d–f) $r_s = 0.05$.

where $\tilde{g}$ is the magnitude of the gravitational acceleration. The momentum and mass conservation equations in dimensionless form are

$$\mathrm{Re}\left(\frac{\partial \mathbf{v}}{\partial t} + \mathbf{v}\cdot\nabla\mathbf{v}\right) = \nabla\cdot\mathbf{T} + \mathrm{St}\mathbf{g}, \tag{2}$$

$$\nabla\cdot\mathbf{v} = 0, \tag{3}$$

where $\mathbf{v}$ is the velocity, $\mathbf{T} = -p\mathbf{I} + \mu(\dot{\gamma})[\nabla\mathbf{v} + (\nabla\mathbf{v})^T]$ is the total stress tensor, $\mathbf{I}$ is the identity tensor, p is the pressure, and $\mathbf{g}$ is a unit vector in the direction of the gravitational field. The tildes have been dropped because all variables are now dimensionless.

In the present paper, we neglect inertial and gravitational forces, i.e., Re $= 0$ and St $= 0$. This is generally valid for imprint lithography (Re $\sim 10^{-4}$ and St $\sim 10^{-3}$) [31] and commonly applied when studying liquid flows in gravure processes [40,41,45]. With these simplifications, Eq. (2) becomes

$$\nabla p = \nabla\cdot\mu(\dot{\gamma})[\nabla\mathbf{v} + (\nabla\mathbf{v})^T]. \tag{4}$$

For the first model problem [Fig. 2(a)], liquid is driven into the cavity solely by an imposed constant pressure drop, $\Delta p = p_{\mathrm{inlet}} - p_{\mathrm{outlet}}$. In this configuration, the characteristic velocity $\tilde{U}_c$ is taken as the mean velocity along the points $p_1 - p_2$ shown in Fig. 2(a) at the first time step of calculation (Sec. II B). For the second model problem [Fig. 2(b)], liquid is driven into the cavity by Δp as well as horizontal motion of the plate, and $\tilde{U}_c$ is chosen as the plate velocity $\tilde{U}$.

At the liquid-air interface, the kinematic and interfacial stress boundary conditions are applied:

$$\mathbf{n}\cdot(\mathbf{v} - \dot{\mathbf{x}}) = 0, \tag{5}$$

$$\mathbf{n}\cdot\mathbf{T} = -\frac{\kappa}{\mathrm{Ca}}\mathbf{n}, \tag{6}$$

where $\mathbf{n}$ is the outward unit normal to the interface, $\dot{\mathbf{x}}$ is the interface velocity, $\kappa = \nabla_s\cdot\mathbf{n}$ is the curvature of the interface, $\nabla_s = (\mathbf{I} - \mathbf{nn})\cdot\nabla$ is the surface gradient operator, and Ca is the capillary number which characterizes the relative importance of viscous forces and surface-tension forces:

$$\mathrm{Ca} = \tilde{\mu}_0\tilde{U}_c/\tilde{\sigma}. \tag{7}$$

The dynamics of the air surrounding the liquid are neglected. For the inlet boundary condition in Fig. 2, the flow is assumed to be well developed and a constant pressure is imposed:

$$\mathbf{n}\cdot\mathbf{T} = -p\mathbf{n} + \mu(\dot{\gamma})\mathbf{n}\cdot(\nabla\mathbf{v})^T. \tag{8}$$

TABLE I. Parameters used in Eq. (1) to describe different cavity geometries with $r_c = 2.5$. Corner points p_2 and p_3, shown in Fig. 2, denote the initial positions (x, y) used in the calculations.

δ	0.6	0.7	0.8	0.9	1.0	0.6	0.7	0.8	0.9	1.0	1.2
r_s	0.05	0.05	0.05	0.05	0.05	0.1	0.1	0.1	0.1	0.1	0.2
p_2	(1.0, 1.0)	(0.9, 1.0)	(0.8, 1.0)	(0.7, 1.0)	(0.6, 1.0)	(1.0, 1.0)	(0.9, 1.0)	(0.8, 1.0)	(0.7, 1.0)	(0.6, 1.0)	(0.4, 1.0)
p_3	(1.3, 1.0)	(1.2, 1.0)	(1.1, 1.0)	(1.0, 1.0)	(0.9, 1.0)	(1.3, 1.0))	(1.2, 1.0)	(1.1, 1.0)	(1.0, 1.0)	(0.9, 1.0)	(0.7, 1.0)

At the solid surfaces, no-penetration and no-slip boundary conditions are satisfied:

$$\mathbf{n}_{\text{wall}} \cdot \mathbf{v} = 0, \tag{9}$$

$$\mathbf{t}_{\text{wall}} \cdot \mathbf{v} = \begin{cases} 1 & \text{at the moving plate,} \\ 0 & \text{at the cavity wall,} \end{cases} \tag{10}$$

where $\mathbf{t}_{\text{wall}}$ and $\mathbf{n}_{\text{wall}}$ (which points toward the liquid phase) are the tangent and normal vectors at the solid surface. In the first model problem [Fig. 2(a)], the dynamic contact line is made to move freely along the plate and cavity wall by imposing a Navier-slip boundary condition to replace Eq. (10) along with a constant contact angle θ at the contact line:

$$\mathbf{t}_{\text{wall}} \cdot (\mathbf{n}_{\text{wall}} \cdot \mathbf{T}) = \frac{1}{\beta} \mathbf{t}_{\text{wall}} \cdot (\mathbf{v} - \mathbf{v}_{\text{wall}}), \tag{11}$$

$$\mathbf{n}_{\text{wall}} \cdot \mathbf{n}_{\text{interface}} = \cos\theta, \tag{12}$$

where β is a dimensionless slip coefficient and $\mathbf{v}_{\text{wall}}$ is the wall velocity. In the second model problem [Fig. 2(b)], the contact line on the horizontal plate is assumed to be pinned and move with the plate velocity while the contact line on the cavity moves freely. Following our previous work [40,41,45–48], $\beta = 10^{10}$ is used for all calculations to produce a shear-stress-free contact line. The results are essentially insensitive to the slip-coefficient value down to $\beta = 10$.

B. Solution method

Equations (3)–(12) are solved with the Galerkin finite-element method. Equations (11) and (12) are only applied at the node which is on the contact line while the no-slip condition is imposed elsewhere along the solid surfaces. Therefore, the effective slip length is less than the element size [40,41,45–47]. We note that while a constant value of β is used in this paper, the slip length for shear-thinning liquids could vary with the deformation rate due to the change of liquid viscosity [49,50]. To isolate the effect of other problem parameters, we use a constant value of β in this paper. The moving interface is tracked with elliptic mesh generation and time integration is performed with a second-order adaptive scheme [51]. Details of the numerical methods used are discussed in our prior work [41].

In our calculations, the computational domain is discretized with 30 elements in the x direction and 35 elements in the y direction. In this paper, cavities with different widths and steepnesses are used to simulate various cavity geometries [10] and the parameters defining the initial liquid domain are shown in Table I. Similar initial liquid domains were also used in prior work [31,34]. The initial coordinates of p_1 and p_4 (Fig. 2) are located vertically above p_2 and p_3, respectively, by a distance H.

C. Constitutive model

For describing shear thinning, we choose the commonly used Carreau-type model [52]:

$$\mu(\dot{\gamma}) = (1 - \beta_s)[1 + (\text{De}\dot{\gamma})^2]^{(n-1)/2} + \beta_s, \tag{13}$$

where $\beta_s = \tilde{\mu}_\infty/\tilde{\mu}_0 \leqslant 1$ is the ratio of the viscosity at infinite deformation rate $\tilde{\mu}_\infty$ to that at zero deformation rate, $\mathrm{De} = \tilde{\lambda}\tilde{U}_c/\tilde{D}$ is the Deborah number which characterizes the time scales for liquid relaxation and deformation where $\tilde{\lambda}$ is a time constant (the reciprocal of the characteristic deformation rate where shear thinning becomes significant), and $n \leqslant 1$ is a power-law exponent determining the slope of the thinning regime. The deformation rate, $\dot{\gamma} = \sqrt{2II_{\mathbf{D}}}$, is related to the square root of the second invariant of the rate-of-deformation tensor $\mathbf{D} = \frac{1}{2}[\nabla\mathbf{v} + (\nabla\mathbf{v})^T]$. In a Cartesian coordinate system, the deformation rate is

$$\dot{\gamma} = \left[2\left(\frac{\partial v_x}{\partial x}\right)^2 + \left(\frac{\partial v_x}{\partial y} + \frac{\partial v_y}{\partial x}\right)^2 + 2\left(\frac{\partial v_y}{\partial y}\right)^2\right]^{1/2}, \tag{14}$$

where v_x and v_y are the horizontal and vertical components of the velocity vector, respectively. While n is typically smaller than 0.5 and β_s could vary from 0.01 to 0.5 for different liquids [52,53], we choose $n = 0.5$ and $\beta_s = 0.1$ as representative parameters in this paper to study shear-thinning effects.

III. PRESSURE-DRIVEN FILLING

In this section, we probe the effects of geometric parameters, surface wettability, and Ca on cavity filling for the first model problem [Fig. 2(a)], which is relevant to imprint lithography, microfluidics, and porous-media flow (Sec. I). The case of Newtonian liquids is discussed first (Sec. III A), followed by an investigation of shear-thinning liquids (Sec. III B).

A. Results: Newtonian liquids

Figure 3 compares the temporal evolution of pressure contours for cavities with the same width $W = 0.8$ and spacing between the cavity and plate $H = 0.35$ but with different steepnesses at Ca $= 0.15$. The contact angle of the cavity θ_c is the same as that of the plate θ_p and is equal to 50°. We choose these contact angles as representative values and will later discuss the influence of wettability differences.

At an early time ($t = 1.7$), Fig. 3(a) indicates that significant pressure gradients are present near both dynamic contact lines as liquid is driven into the cavity ($r_s = 0.1$). These pressure gradients arise when the liquid-air interface deforms to satisfy the specified value of the contact angle, and drive the contact line to slip along the surfaces [Fig. 3(b)]. At a later time ($t = 10.1$), Fig. 3(c) shows that the contact line on the cavity passes over the entire cavity, leading to complete filling.

It is noted that the contact line moves from the cavity bottom [Fig. 3(b)] to the upper-right cavity corner [Fig. 3(c)] within a short time. This is because when the contact line moves along the cavity bottom pronounced pressure gradients resulting from a significantly deformed liquid-air interface enhance contact-line motion. This causes the interface to reconfigure, preventing it from touching the upper-right corner and avoiding air entrapment. Such interface reconfiguration is also reported in prior numerical studies [31,37].

For a steeper cavity (smaller r_s; here, $r_s = 0.05$), significant pressure gradients are also observed at an early time [$t = 1.7$, Fig. 3(d)]. As time progresses, Fig. 3(e) indicates that a cavity with steeper walls causes the contact line on the cavity to slip less compared to what is seen in Fig. 3(b). This is because the liquid-air interface deforms less to maintain a constant contact angle when wall steepness increases [40]. As a result, the liquid-air interface touches the upper-right cavity corner before the contact line can slip down to the cavity bottom, resulting in air entrapment [Fig. 3(f)].

Figure 4 shows the temporal evolution of pressure contours for the case with a larger spacing ($H = 0.5$). Here, a cavity with $W = 0.8$ and $r_s = 0.1$ is studied. For a fixed applied pressure drop, the initial mean velocity at the inlet would increase as the spacing (gap width) increases. Since this velocity is taken as the characteristic velocity, the capillary number for $H = 0.5$ (Ca $= 0.31$) is larger than the value for $H = 0.35$ (Fig. 3, Ca $= 0.15$). Because the pressure scale also involves this velocity, the dimensionless pressure drop is $\Delta p = 90.0$, 30.1, and 14.5 for $H = 0.2$, 0.35, and 0.5,

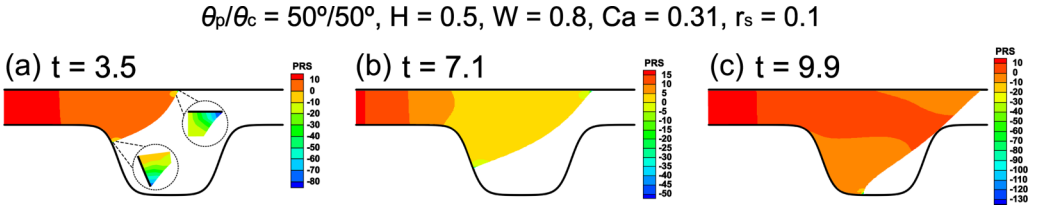

FIG. 4. Contours of dimensionless pressure for Newtonian liquids being filled into a cavity with $\theta_p/\theta_c = 50^\circ/50^\circ$, $H = 0.5$, $W = 0.8$, Ca $= 0.31$, and $r_s = 0.1$ at different times: (a) $t = 3.5$, (b) $t = 7.1$, and (c) $t = 9.9$.

respectively. We note that the corresponding capillary numbers Ca $= 0.05$, 0.15, and 0.31 would have approximately the same values if the characteristic velocity was taken to be that for plane Poiseuille flow in a gap of width $\tilde{H}$ and length corresponding to the initial liquid domain.

Figure 4(a) reveals that significant pressure gradients are seen near dynamic contact lines, but that the liquid-air interface curves outward to the air phase more compared to Fig. 3(a) because of the larger Ca value. The outward-curved interface is still observed as time proceeds [Fig. 4(b)]. At a later time [Fig. 4(c)], the interface touches the upper-right cavity corner, causing air entrapment. These results suggest that increasing H harms cavity filling due to an increase in Ca.

Figures 5(a) and 5(b) summarize the effects of geometric parameters on cavity filling for r_s equal to 0.1 and 0.05, respectively. For cases where incomplete filling occurs, we also give the fraction of the cavity that is filled with liquid when the simulation ends. In Fig. 5(a), it is seen that complete cavity filling occurs for smaller spacings and for cavities with larger width. When W increases, the contact line on the cavity has more time to slip and pass over the entire cavity, thereby preventing the liquid-air interface from hitting the upper-right cavity corner. Similar results indicating that complete filling of cavities with higher aspect ratio (height to width) is more difficult were reported in prior studies [31,37,38]. Note that changing cavity width does not affect the inlet velocity, i.e., cases with different W have the same value of Ca.

For steeper cavities [Fig. 5(b)], the effects of H and W on cavity filling are observed to be the same. However, the boundary between completely and incompletely filled cavities shifts toward the lower right as r_s decreases, meaning that complete filling is achieved for a narrower parameter

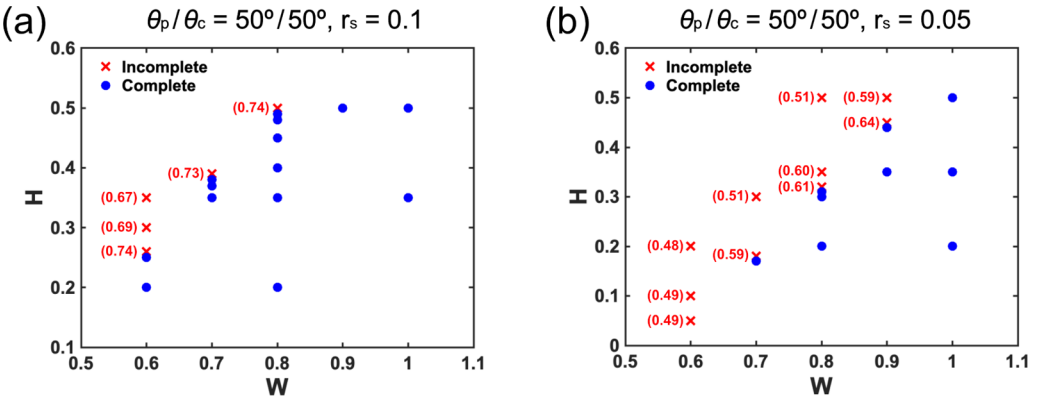

FIG. 5. Effects of geometric parameters on cavity filling for Newtonian liquids with $\theta_p/\theta_c = 50^\circ/50^\circ$ and (a) $r_s = 0.1$ and (b) $r_s = 0.05$. Crosses represent incompletely filled cavities while circles represent completely filled cavities. The capillary numbers are 0.05, 0.15, and 0.31 for $H = 0.2$, 0.35, and 0.5, respectively. The numbers in the panels indicate the fraction of the cavity that is filled with liquid when the simulation ends.

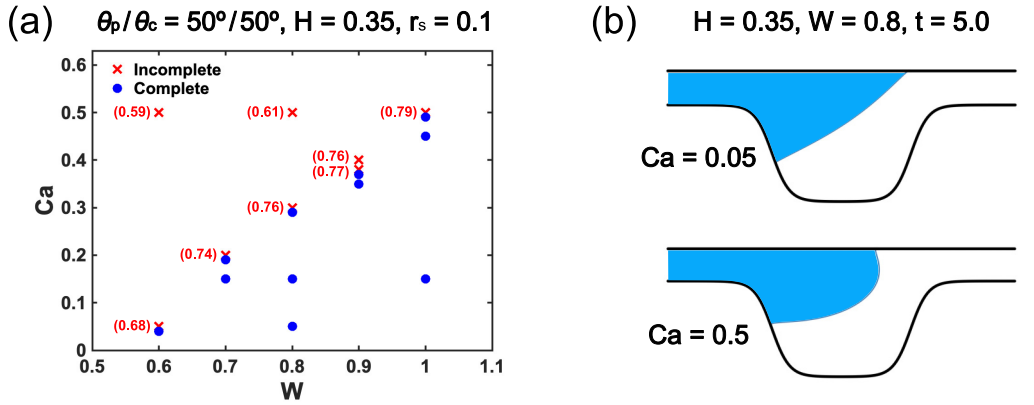

FIG. 6. Results for Newtonian liquids with $\theta_p/\theta_c = 50^\circ/50^\circ$, $H = 0.35$, $r_s = 0.1$, and varying W. Panel (a) shows the influence of Ca on cavity filling. Panel (b) compares the liquid-air interface for cavities with $W = 0.8$ at $t = 5.0$. The numbers in panel (a) indicate the fraction of the cavity that is filled with liquid when the simulation ends.

range. This is due to slower contact-line motion on the cavity when wall steepness increases, as demonstrated in Fig. 3.

In Fig. 6, we examine the influence of Ca on the filling process for cavities with $r_s = 0.1$ and different W while keeping $H = 0.35$. Figure 6(a) shows that complete filling is achieved only for wider cavities at small Ca. The liquid-air interface shapes for different values of Ca at $t = 5.0$ are compared in Fig. 6(b) to rationalize this observation. It is seen that the liquid-air interface curvature is smaller at Ca = 0.05 and becomes curved outward toward the air phase more when Ca increases to 0.5. This is similar to cavity filling with a larger H, in which Ca is raised due to a higher inlet velocity (Fig. 4). Also, Fig. 6(b) indicates that the contact line slips less on the cavity when Ca increases. This is due to stronger viscous resistance relative to the surface-tension forces that drive the flow. As a result, air entrapment is more likely to occur at larger Ca. We note that similar observations of how the interface changes with Ca were reported in prior work simulating 3D cavities [39], implying that the simpler 2D model studied here could be a useful tool for developing physical understanding at lower computational cost.

We now probe the effect of surface wettability on cavity filling. The results for cavities with two steepnesses for $\theta_p/\theta_c = 70^\circ/50^\circ$ and different geometric parameters are shown in Fig. 7. When the plate becomes less wettable (larger θ) than the cavity, Fig. 7(a) shows that the boundary between completely and incompletely filled cavities shifts toward the upper left compared to the case with $\theta_p/\theta_c = 50^\circ/50^\circ$ [Fig. 5(a)], suggesting that complete filling occurs for a broader geometric parameter range. This shift is also seen for steeper cavities in Fig. 7(b) when compared to Fig. 5(b).

To explain the influence of contact angle, Fig. 8(a) compares the horizontal coordinate of the contact lines on both surfaces as time progresses for the case with $H = 0.5$, $W = 0.8$, and $r_s = 0.1$. It is found that the contact-line positions on the cavity for different pairs of contact angles closely follow each other until $t \approx 9.0$. In contrast, the x coordinate of the contact line on the plate for $\theta_p/\theta_c = 70^\circ/50^\circ$ is smaller than that for $\theta_p/\theta_c = 50^\circ/50^\circ$, meaning that increasing the contact angle for the plate causes that contact line to slip more slowly. This is because, when θ increases, the pressure gradients driving contact-line motion are weaker due to a less deformed liquid-air interface near the dynamic contact line. As a result, making the plate less wettable than the cavity avoids air entrapment and results in complete filling [Fig. 8(b)].

The above analyses also imply that decreasing the contact angle for the cavity generally benefits filling by increasing the wettability difference between the cavity and plate. Similar observations regarding the influence of cavity wettability were reported in previous numerical studies [37,38].

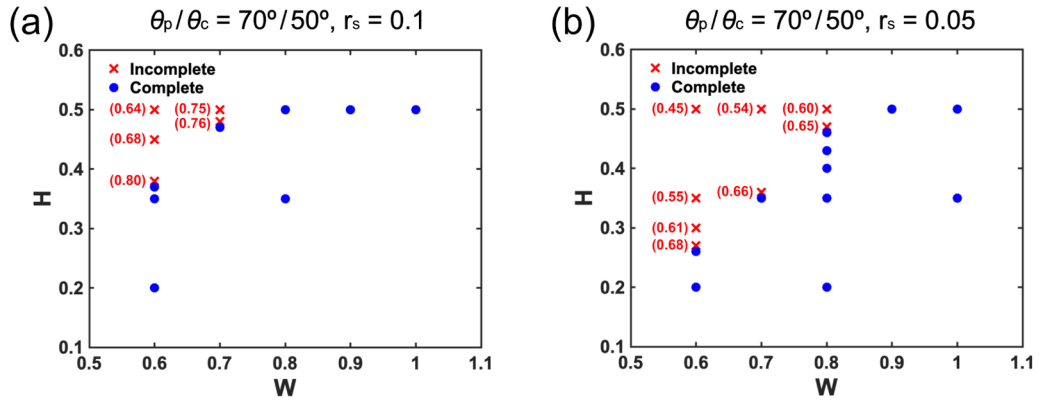

FIG. 7. Effects of geometric parameters on cavity filling for Newtonian liquids with $\theta_p/\theta_c = 70^\circ/50^\circ$ for (a) $r_s = 0.1$ and (b) $r_s = 0.05$. The capillary numbers are 0.05, 0.15, and 0.31 for $H = 0.2$, 0.35, and 0.5, respectively. The numbers in the panels indicate the fraction of the cavity that is filled with liquid when the simulation ends.

For applications such as UV imprint lithography, increasing the contact angle for the plate material or decreasing the contact angle of the cavity might benefit the filling process. However, these wettability changes may affect adhesion of the solidified material, so their influence on the demolding step of imprint lithography also needs to be considered [1,54].

B. Results: Shear-thinning liquids

We now consider shear-thinning liquids. Figure 9 summarizes the effects of geometric parameters on filling for shear-thinning liquids ($n = 0.5$ and $\beta_s = 0.1$) with $r_s = 0.1$ and $\theta_p/\theta_c = 50^\circ/50^\circ$. Recall that the capillary number is defined based on the average velocity at the inlet and the viscosity at zero deformation rate, and the Deborah number is based on the same average velocity (Sec. II A). The values of Ca and De corresponding to different H in Fig. 9 are shown in Table II. As for Newtonian liquids, variation in W does not influence the inlet velocity. Thus, Ca and De do not vary with W. We can also calculate an effective capillary number, $\mathrm{Ca}_{\mathrm{eff}}$, based on a characteristic shear

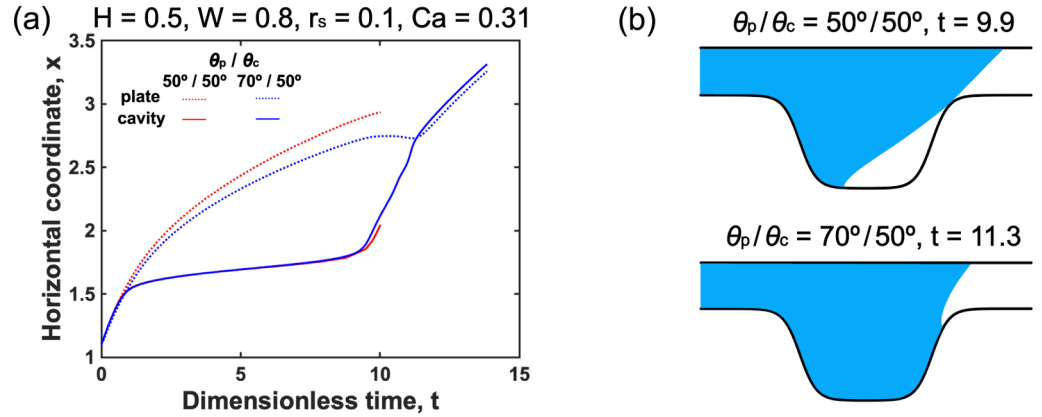

FIG. 8. Results for Newtonian liquids with $H = 0.5$, $W = 0.8$, Ca = 0.31, and $r_s = 0.1$. Panel (a) compares the temporal evolution of contact-line positions in the x direction for $\theta_p/\theta_c = 50^\circ/50^\circ$ and $70^\circ/50^\circ$. Panel (b) shows the liquid-air interface for incompletely (top) and completely (bottom) filled cases.

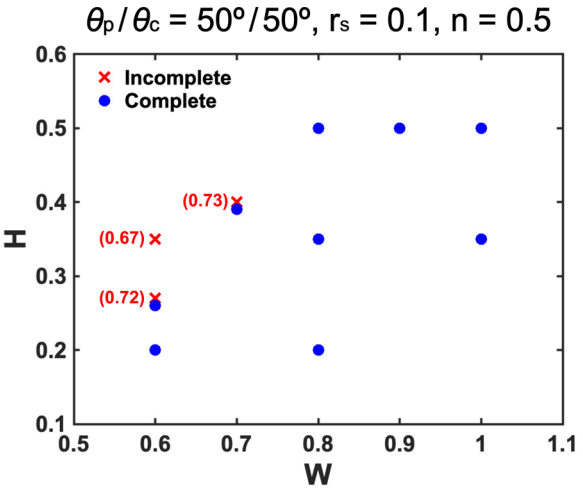

FIG. 9. Effects of geometric parameters on cavity filling for shear-thinning liquids ($n = 0.5$ and $\beta_s = 0.1$) with $\theta_p/\theta_c = 50^\circ/50^\circ$ and $r_s = 0.1$. The numbers in the panel indicate the fraction of the cavity that is filled with liquid when the simulation ends.

rate, which we take to be the average velocity at the inlet divided by the cavity depth. This is also included in Table II to characterize the extent of shear thinning.

In Fig. 9, it is found that shear-thinning liquids show similar results compared to Newtonian liquids [Fig. 5(a)] except for the case where $H = 0.5$ and $W = 0.8$. For this set of geometric parameters, shear-thinning liquids give rise to complete filling whereas Newtonian liquids lead to an incompletely filled cavity. The effects of shear thinning are explained in Fig. 10 by examining the temporal evolution of the pressure and viscosity contours with $\theta_p/\theta_c = 50^\circ/50^\circ$, $H = 0.5$, and $W = 0.8$. We note that although in this case the capillary number for shear-thinning liquids (1.7) is much higher than the value for Newtonian liquids (0.31) the effective capillary number (0.52) is comparable to the Newtonian value.

From Fig. 10(a), the pressure contours indicate that strong pressure gradients are found near both dynamic contact lines with similar magnitudes, analogous to what is seen for the Newtonian case (Fig. 4). The contact-line motion driven by these pressure gradients results in reduced viscosities through increased deformation rates [Eq. (13)], leading to comparable viscosity gradients near both contact lines, as shown in the viscosity contours in Fig. 10(d).

As time progresses, Fig. 10(b) shows that the pressure gradients near the contact line on the cavity become more pronounced than those on the plate. This is because the local liquid-air interface deforms dramatically when the contact line moves from the cavity wall to the cavity bottom. As a result of large deformation, significant viscosity gradients arise near the contact line on the cavity [Fig. 10(e)]. In contrast, the liquid-air interface remains relatively flat as the contact line is approached on the flat plate, leading to weaker pressure and viscosity gradients. Consequently, the contact line on the cavity proceeds much more quickly than that on the plate due to stronger driving

TABLE II. Dimensionless parameters for shear-thinning liquids in Fig. 9 with different H.

H	0.2	0.35	0.5
De	2.9	9.1	18.6
Ca	0.26	0.82	1.7
$\mathrm{Ca}_{\mathrm{eff}}$	0.16	0.33	0.52

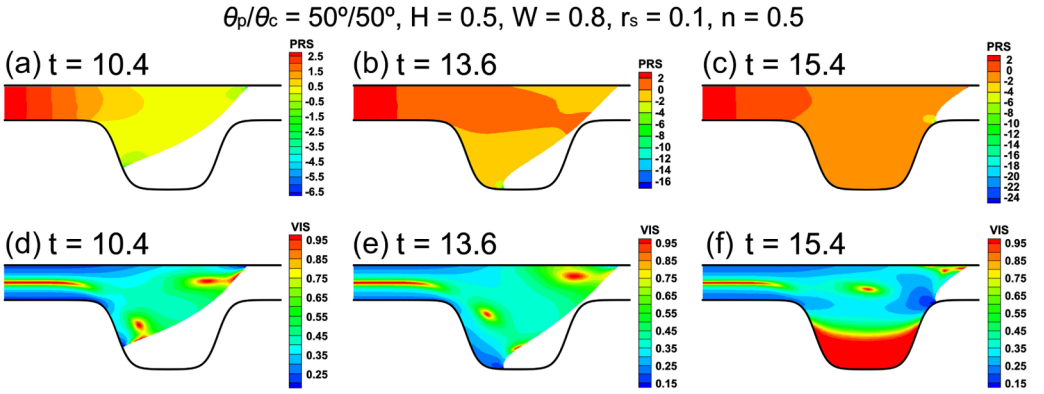

FIG. 10. Contours of dimensionless (a–c) pressure and (d–f) viscosity for shear-thinning liquids with $n = 0.5$, $\beta_s = 0.1$, and De $= 18.6$ being filled into a cavity with $\theta_p/\theta_c = 50^\circ/50^\circ$, $H = 0.5$, $W = 0.8$, Ca $= 1.7$, $\text{Ca}_{\text{eff}} = 0.52$, and $r_s = 0.1$ at different times.

forces and weaker viscous resistance and is able to pass over the entire cavity [Figs. 10(c) and 10(f)]. Thus, a completely filled cavity is observed for shear-thinning liquids (Fig. 9) as opposed to an incompletely filled one for Newtonian liquids [Fig. 5(a)].

Figure 11 demonstrates a similar analysis for the case where $H = 0.35$ and $W = 0.6$ shown in Fig. 9. With this set of geometric parameters, both Newtonian and shear-thinning liquids lead to incomplete filling. From Fig. 11, it is observed that the magnitudes of pressure [Fig. 11(a)] and viscosity [Fig. 11(c)] gradients near both contact lines are close at $t = 4.7$. At a later time ($t = 12.2$) when the liquid-air interface touches the cavity corner, the pressure [Fig. 11(b)] and viscosity [Fig. 11(d)] gradients near both contact lines are still comparable since the contact line remains on the cavity wall.

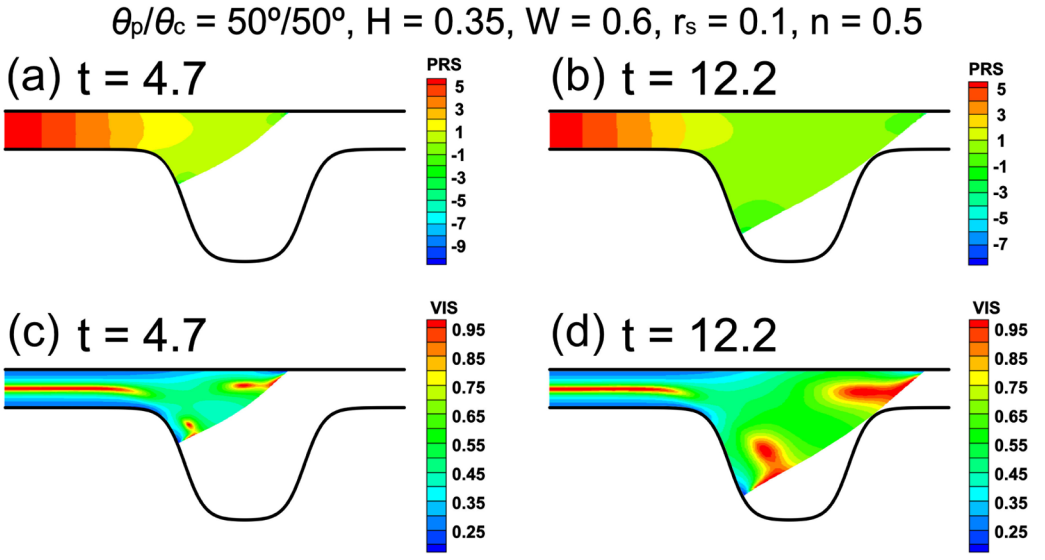

FIG. 11. Contours of dimensionless (a, b) pressure and (c, d) viscosity for shear-thinning liquids with $n = 0.5$, $\beta_s = 0.1$, and De $= 9.1$ being filled into a cavity with $\theta_p/\theta_c = 50^\circ/50^\circ$, $H = 0.35$, $W = 0.6$, Ca $= 0.82$, $\text{Ca}_{\text{eff}} = 0.33$, and $r_s = 0.1$ at different times.

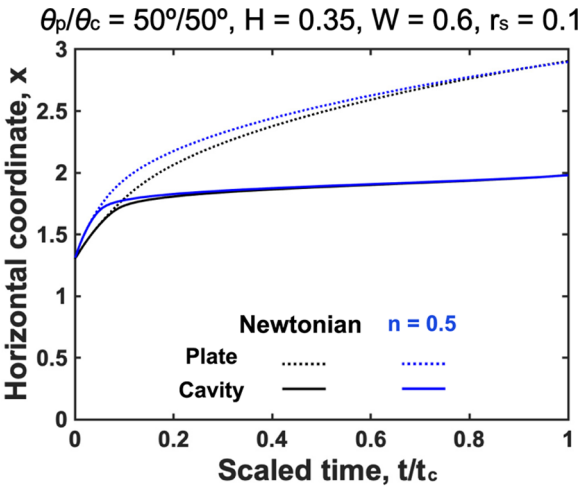

FIG. 12. Temporal evolution of contact-line positions in the x direction with $\theta_p/\theta_c = 50^\circ/50^\circ$, $H = 0.35$, and $W = 0.6$ for Newtonian and shear-thinning liquids. The x axis is scaled by the total time of computation, t_c.

The temporal evolution of the horizontal coordinate of the contact line on both surfaces for Newtonian and shear-thinning liquids with $H = 0.35$ and $W = 0.6$ is compared in Fig. 12. The x axis is the dimensionless time t scaled by the total time of computation t_c. It is seen that when the liquid-air interface reaches the upper-right cavity corner ($t/t_c = 1$) the difference of contact-line position on both surfaces between the Newtonian and shear-thinning cases is nearly indistinguishable. This suggests that without large differences of the pressure and viscosity gradients between two contact lines the contact-line evolution for shear-thinning liquids is analogous to that for Newtonian liquids. Thus, shear thinning has negligible influence on improving cavity filling here (Fig. 11) as opposed to what is seen in Fig. 10.

We note that the above discussion focuses on cases where De is $O(10)$. For cavity filling of shear-thinning liquids with high values of De [e.g., De $> O(10^3)$, results not shown], we find that viscosities in the bulk liquid decrease quickly to the asymptotic value $\tilde{\mu}_\infty$ since the time scale for liquid relaxation is much larger than that for liquid deformation. As a result, the viscosity distribution becomes nearly homogeneous, making the evolution of the filling process analogous to the Newtonian case with the same $\tilde{\mu}_\infty$.

In Sec. III B, shear thinning is shown to improve cavity filling by allowing the contact line on the cavity to move more quickly than that on the plate. This stems from differences in the pressure and viscosity gradients near the contact line between the two surfaces. These results imply that shear thinning could be exploited to avoid air entrapment when Newtonian liquids with the same $\tilde{\mu}_0$ result in an incompletely filled cavity.

IV. BOUNDARY- AND PRESSURE-DRIVEN FILLING

We now consider the model problem where liquid is filled into the cavity by a combination of horizontal plate motion and an imposed pressure gradient [Fig. 2(b)]. In this model problem, which is relevant to gravure processes (Sec. I), the contact line on the plate is pinned and moves with the plate whereas the contact line on the cavity slips freely. Cavity filling with Newtonian liquids is probed for different parameters in Sec. IV A, followed by shear-thinning liquids in Sec. IV B.

A. Results: Newtonian liquids

The cases of cavity filling without an applied pressure drop ($\Delta p = 0$) are examined first. For the following calculations, less steep cavities with $r_s = 0.2$ are used to facilitate the computations and

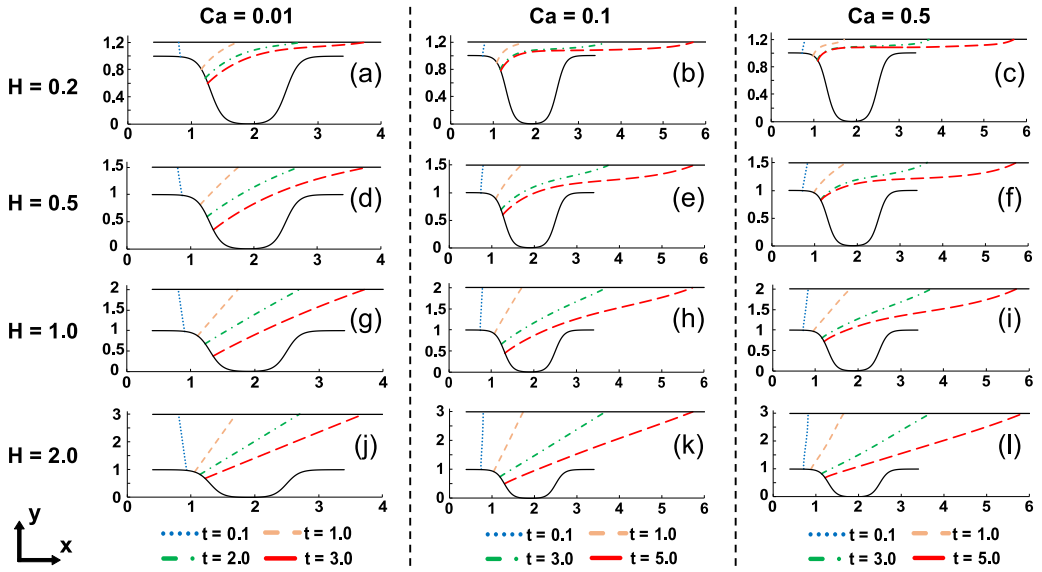

FIG. 13. Temporal evolution of interface shapes for Newtonian liquids with $\theta_c = 70^\circ$; $W = 1.2$; $\Delta p = 0$; Ca $= 0.01$, 0.1, and 0.5; and $r_s = 0.2$ at different spacings: (a–c) $H = 0.2$, (d–f) $H = 0.5$, (g–i) $H = 1.0$, and (j–l) $H = 2.0$.

W is fixed at 1.2. Figure 13 shows the temporal evolution of the liquid-air interface with $\theta_c = 70^\circ$ for different values of H and Ca. Note that Ca is defined based on the plate velocity in this model problem.

For $H = 0.2$ and Ca $= 0.01$, Fig. 13(a) shows that the contact line slips down the cavity as time proceeds and the liquid-air interface remains curved toward the liquid phase. As Ca increases to 0.1, the contact line slips at early times ($t < 3.0$) but starts to pin on the cavity as time progresses [Fig. 13(b)]. When Ca is 0.5, the contact line slips even less because of stronger viscous resistance to contact-line motion [Fig. 13(c)].

When H increases 0.5, Fig. 13(d) shows that the liquid-air interface is less curved and the contact line slips more down the cavity compared to the case where $H = 0.2$ [Fig. 13(a)]. This suggests that increasing H reduces the influence of cavity geometry on the interface curvature and decreases contact-line pinning. In Fig. 13(e), it is seen that the contact line continues to slip down the cavity at $t = 5.0$. In contrast, the contact line pins at this time in Fig. 13(b). When Ca is 0.5, Fig. 13(f) reveals that contact-line pinning occurs at a time similar to what is seen in Fig. 13(c), suggesting that the strong viscous forces dominate over the effect of spacing.

When H equals 1.0, Figs. 13(g)–13(i) indicate that the influence of cavity geometry on the interface curvature is further reduced compared to cases with smaller H. At Ca $= 0.5$, Fig. 13(i) shows that contact-line pinning has not yet been observed at $t = 5.0$, meaning that larger H allows the contact line to slip more. For an even larger spacing $H = 2.0$, the liquid-air interface is seen to be nearly flat as time evolves [Figs. 13(j)–13(l)], suggesting negligible influence of cavity geometry on the interface shape.

To provide a quantitative analysis of how cavity filling is affected by H, the fraction of liquid filled in the cavity, V_f, is plotted as a function of Ca for different values of H in Fig. 14. The quantity V_f is defined as the ratio of the volume of liquid remaining in the cavity ($y \leqslant 1.0$) to the total volume of the cavity when the computation is ended. This corresponds to situations when either (i) the liquid-air interface reaches the upper-right corner of the cavity or (ii) $t = 25$, at which the contact line barely moves along the cavity even as time further progresses. We note that V_f is used

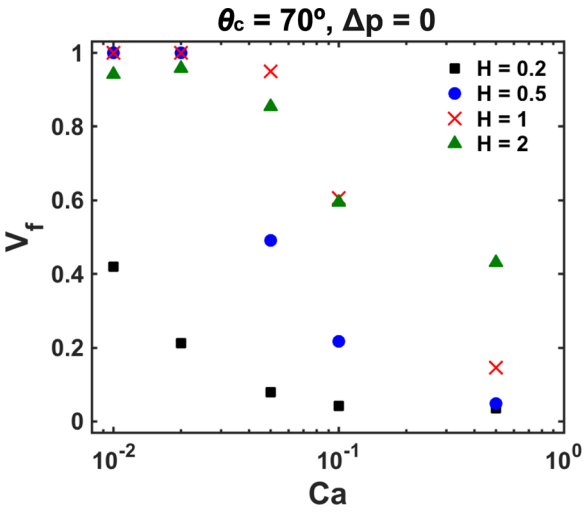

FIG. 14. Relationship between V_f and Ca for Newtonian liquids with $\theta_c = 70^\circ$, $\Delta p = 0$, and different spacings H.

here (Sec. IV) to characterize different extents of contact-line pinning (Fig. 13), which is not seen in Sec. III.

Figure 14 shows that V_f decreases (less liquid filled) with increasing Ca or decreasing H due to weaker contact-line slip along the cavity, as demonstrated in Fig. 13. It is seen that complete filling ($V_f = 1.0$) is only achieved for small values of Ca [$\approx O(10^{-2})$], similar to what was observed in prior experiments with 3D cavities [34]. In Fig. 14, it is also observed that V_f for $H = 2.0$ is smaller than the value for $H = 1.0$ when Ca is less than 0.1, indicating that increasing the spacing between the cavity and plate does not necessarily benefit cavity filling. This is because when H is large enough (e.g., $H = 2.0$) the liquid-air interface close to the upper-right cavity corner is not curved toward the liquid phase [Figs. 13(j)–13(l)], causing it to touch the cavity corner more easily.

We now study the effect of an applied pressure drop on cavity filling. Figure 15 compares the temporal evolution of the liquid-air interface with $\theta_c = 70^\circ$ and $H = 0.2$ for different values of Δp and Ca. For $\Delta p = 0$, Figs. 15(a)–15(c) show a similar trend to what is demonstrated in Figs. 13(a)–

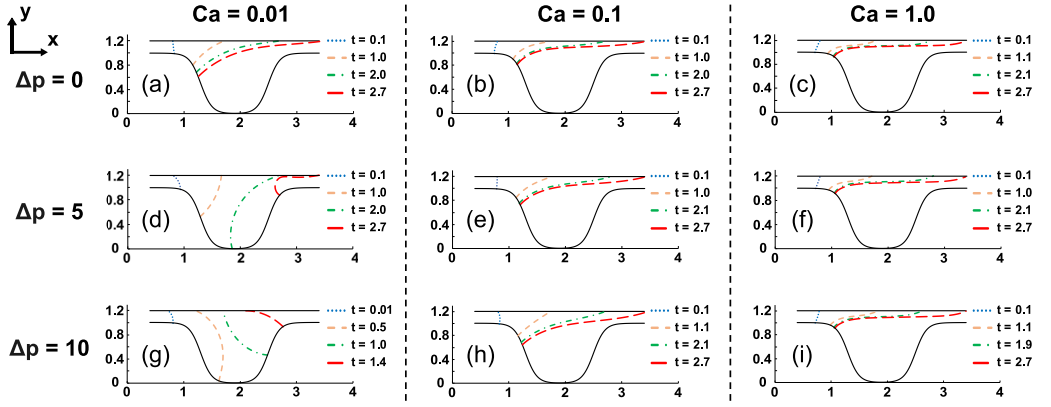

FIG. 15. Temporal evolution of interface shapes for Newtonian liquids with $H = 0.2$; $\theta_c = 70^\circ$; Ca = 0.01, 0.1, and 1; and $r_s = 0.2$ at different pressure drops: (a–c) $\Delta p = 0$, (d–f) $\Delta p = 5$, and (g–i) $\Delta p = 10$.

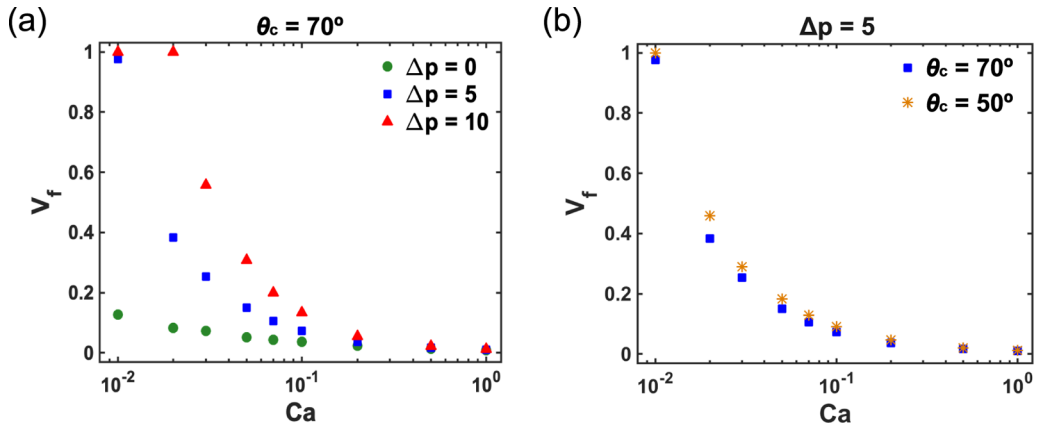

FIG. 16. Relationship between V_f and Ca for Newtonian liquids at $H = 0.2$ with (a) $\theta_c = 70^\circ$ and $\Delta p = 0$, 5, and 10 and (b) $\theta_c = 50$ and 70° and $\Delta p = 5$.

13(c), i.e., the contact line slips down the cavity as time proceeds at small Ca but becomes pinned on the cavity when Ca increases.

When $\Delta p = 5$ and Ca $= 0.01$, Fig. 15(d) indicates that an increase in Δp allows the contact line to slip much further than when $\Delta p = 0$ [Fig. 15(a)] because the driving forces for contact-line motion increase. At larger Ca, Fig. 15(e) shows a similar liquid-air interface evolution as Fig. 15(b), implying that the influence of increased Δp on enhancing contact-line motion is reduced. When Ca increases to 1.0, the contact line slips slightly along the cavity and the difference of interface evolution between Figs. 15(c) and 15(f) is negligible.

With an even larger pressure drop ($\Delta p = 10$) and small Ca, Fig. 15(g) shows that the cavity is filled completely at an earlier time ($t = 1.4$) compared to Fig. 15(d) ($t = 2.7$) due to stronger contact-line motion along the cavity. When Ca increases to 0.1, the enhanced contact-line motion is still observed in Fig. 15(h) but the extent of enhancement is less pronounced than when Ca $= 0.01$. When Ca is 1.0, significant contact-line pinning is observed in Fig. 15(i), as seen in Figs. 15(c) and 15(f). We note that the curved interface shape resulting from early contact-line pinning at large Ca is similar to what was reported in prior 3D simulations [34], suggesting that 2D simulations provide qualitatively similar results.

The results of V_f as a function of Ca for three values of Δp are summarized in Fig. 16(a). Here, V_f is calculated at $t = 2.7$. (By this time, the cavity has either filled or the contact line is effectively pinned, as seen in Fig. 15.) It can be seen that more liquid is filled into the cavity with a larger Δp in general. The influence of Δp on improving cavity filling decreases as Ca increases and becomes negligible when Ca is $O(1)$ because the viscous forces are strong enough to resist contact-line slip, as shown in Fig. 15.

The effect of contact angle on cavity filling with plate motion is illustrated in Fig. 16(b) with $\Delta p = 5$ and $H = 0.2$. It is seen that smaller θ_c results in higher V_f, meaning that more-wettable cavities benefit filling. This is because the liquid-air interface is deformed more significantly near the moving contact line on the cavity when θ_c decreases (Fig. 3), giving rise to stronger pressure gradients to drive contact-line motion. Also, the influence of contact angle on V_f is observed to decrease with increasing Ca, similar to Fig. 16(a).

We note that although other geometric parameters such as cavity width and wall steepness are not examined in this section their influence on cavity filling is expected to be analogous to what is discussed in Sec. III A. For wider (larger W) or less steep (larger r_s) cavities, more liquid can be filled into the cavity because the contact line can slip farther down the cavity.

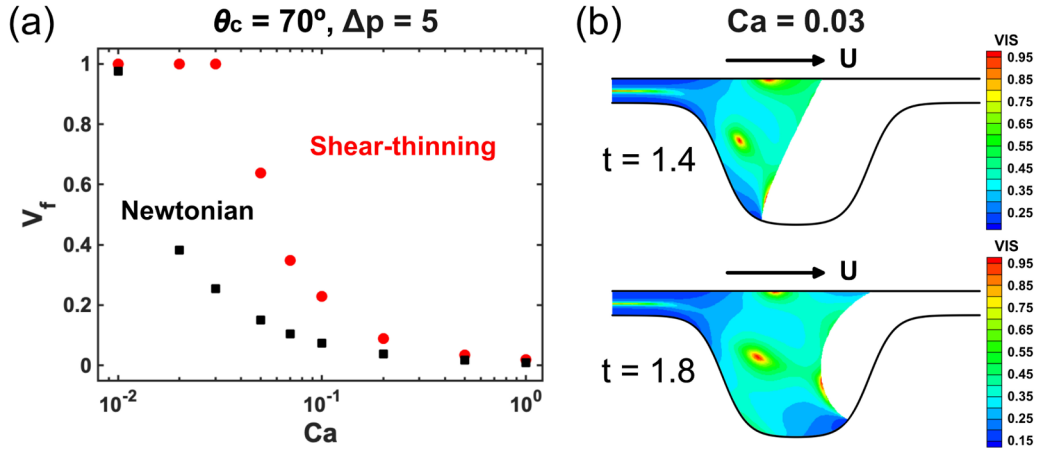

FIG. 17. Panel (a) shows the relationship between V_f and Ca with $H = 0.2$, $\theta_c = 70^\circ$, and $\Delta p = 5$ for Newtonian (squares) and shear-thinning (circles) liquids with $n = 0.5$, $\beta_s = 0.1$, and De $= 1.0$. Panel (b) shows contours of dimensionless viscosity for shear-thinning liquids at Ca $= 0.03$ and different times.

B. Results: Shear-thinning liquids

The filling of shear-thinning liquids is now investigated. Figure 17(a) compares the relationship between V_f and Ca for Newtonian and shear-thinning liquids ($n = 0.5$ and $\beta_s = 0.1$) with $H = 0.2$, $\theta_c = 70^\circ$, and $\Delta p = 5$. Here, De is based on the plate velocity and is chosen as 1.0 for all shear-thinning calculations. Recall that Ca is based on the viscosity at zero deformation rate (Sec. II A) for shear-thinning liquids. Figure 17(a) indicates that shear thinning results in higher V_f than the Newtonian case at the same Ca, meaning that shear-thinning liquids are filled more easily into the cavity.

The viscosity contours for shear-thinning liquids at Ca $= 0.03$ are shown in Fig. 17(b) to illustrate shear-thinning effects. It is observed that as liquid is filled into the cavity reduced viscosities are present near the moving contact line due to pronounced deformation there (similar to Sec. III B). These viscosity gradients allow the contact line to slip more in comparison to the Newtonian case, thereby enhancing cavity filling.

Although we have presented results for fixed values of n and β_s, we expect the amount of liquid filled to increase when the extent of shear thinning increases, i.e., smaller values of n or β_s. This can be rationalized by noting that stronger shear thinning enhances contact-line motion more, as indicated in our prior work concerning liquid emptying from cavities [45]. We also note that for sufficiently large values of De the flow for shear-thinning liquids should behave like Newtonian liquids with the same $\tilde{\mu}_\infty$ since the viscosities are expected to drop close to the value at infinite deformation rate everywhere, as indicated in Sec. III B.

In Sec. IV, we have shown that for cavity filling involving boundary motion complete filling is achieved for Ca values of $O(10^{-2})$ with appropriate spacing between the cavity and plate. Increasing the applied Δp or surface wettability of the cavity allows more liquid to be filled in general by causing stronger contact-line motion on the cavity. At the same Ca, shear thinning is shown to increase the amount of liquid filled compared to the Newtonian case by lowering the viscous resistance to contact-line motion via reduced viscosities near the dynamic contact line.

V. CONCLUSIONS

In this paper, the filling of liquid into a trapezoidal cavity is studied using finite-element simulations for two different model problems. In the first model problem (Sec. III), filling is driven by an imposed pressure drop and involves two moving contact lines. Parametric studies

for Newtonian liquids (Sec. III A) reveal that complete filling is achieved for cavities where the width-to-depth ratio is sufficiently large and for geometries where the spacing between the cavity and plate is sufficiently small relative to cavity depth. In these situations, the contact line is able to slip over the entire cavity. Decreasing Ca, cavity steepness, or contact angle for the cavity enhances contact-line motion along the cavity, thereby reducing the amount of air entrapped.

For shear-thinning liquids (Sec. III B), enhanced contact-line motion is observed on both surfaces due to reduced viscosities. When the contact line slips from the cavity wall to the cavity bottom, significant interface deformation gives rise to large pressure and viscosity gradients near that contact line. This allows the contact line to move more quickly on the cavity than on the plate, resulting in improved filling compared to Newtonian liquids.

In the second model problem (Sec. IV), liquid is driven into the cavity by horizontal plate motion as well as an imposed pressure drop. The conclusions drawn in Sec. III A concerning cavity geometry, surface wettability, and Ca generally apply to this model configuration since the filling process is mainly governed by one moving contact line on the cavity. Our simulations for Newtonian liquids (Sec. IV A) also suggest that increasing the spacing reduces the influence of cavity structure on the interface deformation, which could allow liquid to fill more. Here, shear thinning improves cavity filling through enhanced contact-line slip on the cavity in comparison to Newtonian liquids (Sec. IV B).

The results presented in this paper indicate that shear thinning benefits cavity filling in general. However, it is essential to consider the complex interplay between liquid rheology and different steps of a process to design liquid rheology. For example, shear thinning is found to hinder liquid transfer from cavities in gravure printing [41] but improve the amount of liquid transferred in gravure coating [45]. Shear thinning might also cause underfilled cavities after wiping by a doctor blade in a gravure process [45]. Another important aspect to account for is 3D effects. It has been shown that the edges of 3D cavities could cause contact-line pinning and influence interface deformation significantly [34]. Moreover, as indicated in Sec. I, the interactions between flows in arrays of cavities complicate filling dynamics. Unraveling the influence of complex liquid rheology on these systems requires 3D simulations, which are computationally challenging [55] and an attractive area for future investigation.

ACKNOWLEDGMENT

This work was supported through the Industrial Partnership for Research in Interfacial and Materials Engineering of the University of Minnesota.

[1] P. Yi, H. Wu, C. Zhang, L. Peng, and X. Lai, Roll-to-roll UV imprinting lithography for micro/nanostructures, J. Vac. Sci. Technol. B **33**, 060801 (2015).

[2] H. Wu, P. Yi, L. Peng, and X. Lai, Study on bubble defects in roll-to-roll UV imprinting process for micropyramid arrays. I. Experiments, J. Vac. Sci. Technol. B **34**, 021201 (2016).

[3] Y. Zhou, M. Li, L. Shen, H. Ye, J. Wang, and S. Huang, Effect of resin accumulation on filling process in roll-to-roll UV imprint lithography, J. Vac. Sci. Technol. B **35**, 031602 (2017).

[4] M. Yin, H. Sun, and H. Wang, Resist filling study for UV nanoimprint lithography using stamps with various micro/nano ratios, Micromachines **9**, 335 (2018).

[5] T. Böck and R. Konrad, Chambered doctor blade assembly, US Patent No. 6,539,862B2 (2003).

[6] X. Liang, H. Tan, Z. Fu, and S. Y. Chou, Air bubble formation and dissolution in dispensing nanoimprint lithography, Nanotechnology **18**, 025303 (2006).

[7] R. Kitsomboonloha, S. J. S. Morris, X. Rong, and V. Subramanian, Femtoliter-scale patterning by high-speed, highly scaled inverse gravure printing, Langmuir **28**, 16711 (2012).

[8] H. Ye, L. Shen, M. Li, and Q. Zhang, Bubble defect control in low-cost roll-to-roll ultraviolet imprint lithography, Micro Nano Letters **9**, 28 (2014).

[9] H. Zhang, A. Ramm, S. Lim, W. Xie, B. Y. Ahn, W. Xu, A. Mahajan, W. J. Suszynski, C. Kim, J. A. Lewis, C. D. Frisbie, and L. F. Francis, Wettability contrast gravure printing, Adv. Mater. **27**, 7420 (2015).
[10] G. Grau, J. Cen, H. Kang, R. Kitsomboonloha, W. J. Scheideler, and V. Subramanian, Gravure-printed electronics: Recent progress in tooling development, understanding of printing physics, and realization of printed devices, Flexible and Printed Electronics **1**, 023002 (2016).
[11] H. Jeong, H. Moon, H.-J. Kim, M. Yoon, C.-G. Park, Y. S. Oh, H. J. Sung, D.-G. Choi, and S. Yoo, Spontaneous additive nanopatterning from solution route using selective wetting, ACS Appl. Mater. Interfaces **10**, 26501 (2018).
[12] P. Wiktor, A. Brunner, P. Kahn, J. Qiu, M. Magee, X. Bian, K. Karthikeyan, and J. LaBaer, Microreactor array device, Sci. Rep. **5**, 8736 (2015).
[13] Y. Li, X. Hu, S. Liang, J. Li, and H. Chen, Cleaning of fluid-infused surfaces in microchannels, Langmuir **34**, 12532 (2018).
[14] I. Pereiro, A. Fomitcheva Khartchenko, L. Petrini, and G. V. Kaigala, Nip the bubble in the bud: A guide to avoid gas nucleation in microfluidics, Lab on a Chip **19**, 2296 (2019).
[15] D. Quéré, Non-sticking drops, Rep. Prog. Phys. **68**, 2495 (2005).
[16] J. D. Smith, R. Dhiman, S. Anand, E. Reza-Garduno, R. E. Cohen, G. H. McKinley, and K. K. Varanasi, Droplet mobility on lubricant-impregnated surfaces, Soft Matter **9**, 1772 (2013).
[17] G. McHale, B. V. Orme, G. G. Wells, and R. Ledesma-Aguilar, Apparent contact angles on lubricant-impregnated surfaces/SLIPS: From superhydrophobicity to electrowetting, Langmuir **35**, 4197 (2019).
[18] A. Gupta, H. Lee, and P. S. Doyle, Controlled liquid entrapment over patterned sidewalls in confined geometries, Phys. Rev. Fluids **2**, 094007 (2017).
[19] C. K. Sahu and M. R. Flynn, The effect of sudden permeability changes in porous media filling box flows, Transp. Porous Media **119**, 95 (2017).
[20] A. Gupta, H. Lee, and P. S. Doyle, Oil recovery from micropatterned triangular troughs during a surfactant flood, Langmuir **34**, 10644 (2018).
[21] K. Singh, M. Jung, M. Brinkmann, and R. Seemann, Capillary-dominated fluid displacement in porous media, Annu. Rev. Fluid Mech. **51**, 429 (2019).
[22] F. Goldschmidtboeing, M. Rabold, and P. Woias, Strategies for void-free liquid filling of micro cavities, J. Micromech. Microeng. **16**, 1321 (2006).
[23] D. Seo, A. M. Schrader, S.-Y. Chen, Y. Kaufman, T. R. Cristiani, S. H. Page, P. H. Koenig, Y. Gizaw, D. W. Lee, and J. N. Israelachvili, Rates of cavity filling by liquids, Proc. Natl. Acad. Sci. USA **115**, 8070 (2018).
[24] L. W. Schwartz, P. Moussallp, P. Campbell, and R. R. Eley, Numerical modelling of liquid withdrawal from gravure cavities in coating operations, Chem. Eng. Res. Des. **76**, 22 (1998).
[25] L. W. Schwartz, Numerical modeling of liquid withdrawal from gravure cavities in coating operations; the effect of cell pattern, J. Eng. Math. **42**, 243 (2002).
[26] P. S. H. Forsberg, C. Priest, M. Brinkmann, R. Sedev, and J. Ralston, Contact line pinning on microstructured surfaces for liquids in the Wenzel state, Langmuir **26**, 860 (2010).
[27] J. Wang, M. Do-Quang, J. J. Cannon, F. Yue, Y. Suzuki, G. Amberg, and J. Shiomi, Surface structure determines dynamic wetting, Sci. Rep. **5**, 8474 (2015).
[28] L. Schneider, M. Laustsen, N. Mandsberg, and R. Taboryski, The influence of structure heights and opening angles of micro- and nanocones on the macroscopic surface wetting properties, Sci. Rep. **6**, 21400 (2016).
[29] F.-C. Yang, X.-P. Chen, and P. Yue, Surface roughness effects on contact line motion with small capillary number, Phys. Fluids **30**, 012106 (2018).
[30] H. D. Rowland, A. C. Sun, P. R. Schunk, and W. P. King, Impact of polymer film thickness and cavity size on polymer flow during embossing: toward process design rules for nanoimprint lithography, J. Micromech. Microeng. **15**, 2414 (2005).
[31] S. Reddy, P. R. Schunk, and R. T. Bonnecaze, Dynamics of low capillary number interfaces moving through sharp features, Phys. Fluids **17**, 122104 (2005).
[32] N. Kooy, K. Mohamed, L. T. Pin, and O. S. Guan, A review of roll-to-roll nanoimprint lithography, Nanoscale Res. Lett. **9**, 320 (2014).

[33] A. Jain, A. Spann, A. Cochrane, P. R. Schunk, and R. T. Bonnecaze, Fluid flow in UV nanoimprint lithography with patterned templates, Microelectron. Eng. **173**, 62 (2017).
[34] J. Cen, R. Kitsomboonloha, and V. Subramanian, Cell filling in gravure printing for printed electronics, Langmuir **30**, 13716 (2014).
[35] S. Dodds, M. S. Carvalho, and S. Kumar, The dynamics of three-dimensional liquid bridges with pinned and moving contact lines, J. Fluid Mech. **707**, 521 (2012).
[36] S. Kumar, Liquid transfer in printing processes: Liquid bridges with moving contact lines, Annu. Rev. Fluid Mech. **47**, 67 (2015).
[37] K.-D. Kim, H.-J. Kwon, D.-G. Choi, J.-H. Jeong, and E.-S. Lee, Resist flow behavior in ultraviolet nanoimprint lithography as a function of contact angle with stamp and substrate, Jpn. J. Appl. Phys. **47**, 8648 (2008).
[38] D. Morihara, H. Hiroshima, and Y. Hirai, Numerical study on bubble trapping in UV-nanoimprint lithography, Microelectron. Eng. A **86**, 684 (2009).
[39] L. Peng, H. Wu, P. Yi, and X. Lai, Study on bubble defects in roll-to-roll UV imprinting process for micropyramid arrays II: Numerical study, J. Vac. Sci. Technol. B **34**, 051203 (2016).
[40] S. Dodds, M. S. Carvalho, and S. Kumar, Stretching and slipping of liquid bridges near plates and cavities, Phys. Fluids **21**, 092103 (2009).
[41] J.-T. Wu, M. S. Carvalho, and S. Kumar, Transfer of rate-thinning and rate-thickening liquids between separating plates and cavities, J. Non-Newtonian Fluid Mech. **255**, 57 (2018).
[42] C. M. Gramlich, A. Mazouchi, and G. M. Homsy, Time-dependent free surface Stokes flow with a moving contact line. II. Flow over wedges and trenches, Phys. Fluids **16**, 1660 (2004).
[43] M. J. Kim, S. Song, S. J. Kwon, and H. H. Lee, Trapezoidal structure for residue-free filling and patterning, J. Phys. Chem. C **111**, 1140 (2007).
[44] C. Chung and S. Kumar, Emptying of viscoelastic liquids from model gravure cells, J. Non-Newtonian Fluid Mech. **221**, 1 (2015).
[45] J.-T. Wu, M. S. Carvalho, and S. Kumar, Emptying of gravure cavities containing shear-thinning and shear-thickening liquids, J. Non-Newtonian Fluid Mech. **268**, 46 (2019).
[46] S. Dodds, M. S. Carvalho, and S. Kumar, Stretching liquid bridges with moving contact lines: The role of inertia, Phys. Fluids **23**, 092101 (2011).
[47] C.-H. Huang, M. S. Carvalho, and S. Kumar, Stretching liquid bridges with moving contact lines: Comparison of liquid-transfer predictions and experiments, Soft Matter **12**, 7457 (2016).
[48] J.-T. Wu, M. S. Carvalho, and S. Kumar, Effects of shear and extensional rheology on liquid transfer between two flat surfaces, J. Non-Newtonian Fluid Mech. **274**, 104173 (2019).
[49] A. S. Haase, J. A. Wood, L. M. J. Sprakel, and R. G. H. Lammertink, Inelastic non-Newtonian flow over heterogeneously slippery surfaces, Phys. Rev. E **95**, 023105 (2017).
[50] S. Patlazhan and S. Vagner, Apparent slip of shear thinning fluid in a microchannel with a superhydrophobic wall, Phys. Rev. E **96**, 013104 (2017).
[51] P. M. Gresho, R. L. Lee, and R. L. Sani, *On the Time-Dependent Solution of the Incompressible Navier-Stokes Equations in Two and Three Dimensions* (Pineridge, Swansea, 1980), pp. 27–79.
[52] P. J. Carreau, D. D. Kee, and M. Daroux, An analysis of the viscous behaviour of polymeric solutions, Can. J. of Chem. Eng. **57**, 135 (1979).
[53] K. Ankireddy, S. Vunnam, J. Kellar, and W. Cross, Highly conductive short chain carboxylic acid encapsulated silver nanoparticle based inks for direct write technology applications, J. Mater. Chem. C **1**, 572 (2013).
[54] J. Perumal, T. H. Yoon, H. S. Jang, J. J. Lee, and D. P. Kim, Adhesion force measurement between the stamp and the resin in ultraviolet nanoimprint lithography-an investigative approach, Nanotechnology **20**, 055704 (2009).
[55] J. M. R. Marín, H. K. Rasmussen, and O. Hassager, 3D simulation of nano-imprint lithography, Nanoscale Res. Lett. **5**, 274 (2010).